Research Article | Open Access

Greenverse Science

Chen *et al. Greenverse Sci.* **2026**, *1*, 20 **DOI:**10.20517/greenvsci.2026.19

Selective persulfate activation over iron-alloy-based carbon aerogels

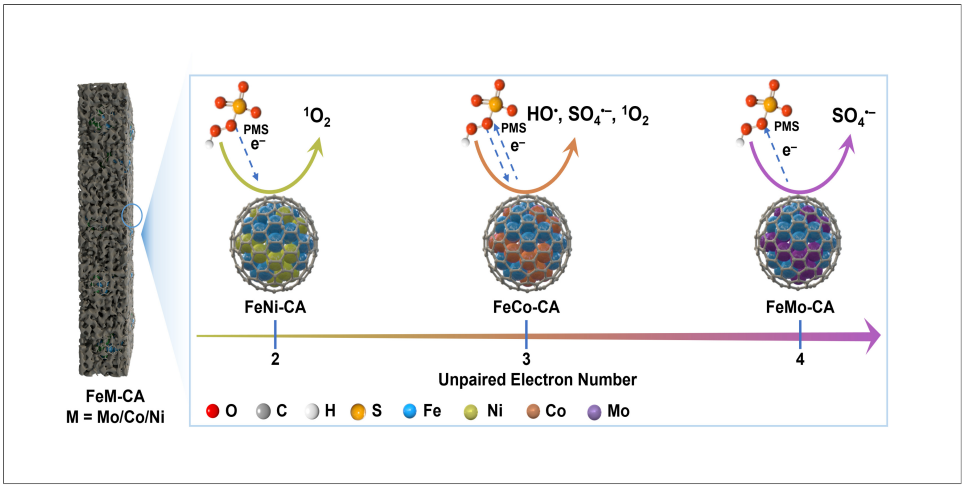
Min Chen[#], Yue Dou[#], Xu Liu, Yanchao Li, Hongying Zhao[*]

Keywords:
Peroxymonosulfate activation, reactive oxygen species, alloy, emerging contaminant

Citation: Chen, M.; Dou, Y.; Liu, X.; Li, Y.; Zhao, H. Selective persulfate activation over iron-alloy-based carbon aerogels. *Greenverse Sci.* **2026**, *1*, 20. https://dx.doi.org/10.20517/greenvsci.2026.19

Received: 13 Aug 2026 **First Decision:** 30 Sep 2026 **Revised:** 12 Nov 2026 **Accepted:** 16 Nov 2026 **Published:** 27 Nov 2026

Academic Editor: Dengsong Zhang **Copy Editor:** Tong Wang **Production Editor:** Tong Wang



Abstract

Emerging contaminants (ECs) have raised concerns because of their high biotoxicity and environmental persistence, which pose significant threats to ecosystems and public health. Peroxymonosulfate-based advanced oxidation processes (PMS-AOPs) offer an efficient strategy for the degradation of ECs by generating diverse reactive oxygen species (ROS). Nevertheless, high-temperature pyrolysis of carbon-based materials can produce diverse surface-active sites that are difficult to control, making it challenging to regulate PMS activation pathways and selectively generate ROS. Hence, this work developed integrated Fe-based alloy-doped carbon aerogels (FeM-CA, M = Mo/Co/Ni) as cathodes to electro-activate PMS. Electron paramagnetic resonance (EPR) and quenching experiments indicated that the FeMo-CA/PMS and FeNi-CA/PMS systems selectively generated $SO_4^{•-}$ and $^1O_2$, respectively, while $HO^•$, $SO_4^{•-}$, and $^1O_2$ coexisted in the FeCo-CA/PMS system. Additionally, temperature-dependent magnetic susceptibility measurements and *in situ* Raman spectroscopy collectively demonstrated that the introduced secondary metals modulated the electron density of alloy centers, thereby regulating the PMS activation pathways. Particularly, FeMo-CA, with abundant unpaired electrons (3.87), promoted the cleavage of the O–O bond in PMS via a radical pathway, generating $SO_4^{•-}$. In contrast, electron-deficient FeNi-CA, with fewer unpaired electrons (2.05), tended to withdraw

Shanghai Key Lab of Chemical Assessment and Sustainability, Key Laboratory of Yangtze River Water Environment, School of Chemical Science and Engineering, Tongji University, Shanghai 200092, China.
[#]These authors contributed equally to this work.

[*]**Correspondence to:** Prof. Hongying Zhao, Shanghai Key Lab of Chemical Assessment and Sustainability, Key Laboratory of Yangtze River Water Environment, School of Chemical Science and Engineering, Tongji University, Shanghai 200092, China. E-mail: hyzhao@tongji.edu.cn

electrons from PMS, inducing a non-radical route dominated by $^1O_2$. FeCo-CA, with an intermediate number of unpaired electrons (2.84), supported the coexistence of radical and non-radical pathways, thereby generating multiple ROS. Furthermore, the catalytic performance and anti-interference capability of FeCo-CA were assessed, demonstrating its promising potential for practical water treatment. This study provided a theoretical basis for catalyst design for selective PMS activation based on the electronic structure of active sites.

INTRODUCTION

In recent years, emerging contaminants (ECs), such as perfluorinated compounds, antibiotics and other synthetic chemicals, pose potential threats to ecosystems and human health due to their environmental persistence and bioaccumulation potential[1-3]. Unlike conventional pollutants, which are often present at high concentrations, ECs are frequently detected at trace levels (ng·L^{-1}-μg·L^{-1}) in complex water matrices[4]. Current water-treatment technologies, including biological processes, membrane separation, adsorption, and disinfection, are insufficient to completely eliminate ECs. Advanced oxidation processes (AOPs) are effective in degrading and mineralizing nonbiodegradable, toxic organic pollutants by generating highly reactive oxygen species (ROS, e.g., HO$^•$) through the activation of oxidants such as hydrogen peroxide, persulfates, peracetic acid, and ozone. These processes are widely used in water purification[5-10]. However, HO$^•$ reactivity is markedly limited in real water matrices because background constituents, including natural organic matter (NOM) and coexisting inorganic anions (carbonate and phosphate), competitively quench HO$^•$. Consequently, selective degradation of target contaminants in complex aqueous environments is still a scientific challenge.

Peroxymonosulfate-based advanced oxidation processes (PMS-AOPs) have emerged as promising strategies for water treatment and can generate diverse ROS via both radical and non-radical pathways to efficiently eliminate organic contaminants[11-13]. In the radical pathway, energy input or electron transfer cleaves the peroxo bond (O–O) in PMS, thereby producing HO$^•$ and/or $SO_4^{•-}$ to degrade pollutants (Eqs. 1-3). By contrast, the non-radical pathway offers moderate oxidizing power, high selectivity, and robust matrix tolerance. It may involve the generation of singlet oxygen ($^1O_2$; Eqs. 4-6), high-valent metal-oxo species (HVMOs), electron-transfer pathways (ETPs), the direct oxidative transfer process (DOTP), and the organic carbon transfer process (OCTP)[14-16]. Nevertheless, most PMS-AOP systems have been reported to involve the coexistence and interplay of radical and non-radical pathways, which can limit the selective removal of target contaminants in complex water matrices[17-22]. Therefore, it is critical to achieve the selective generation of desired ROS in PMS-AOPs systems.

$$HSO_5^- + e^- \rightarrow SO_4^{\cdot-} + OH^- \quad (1)$$

$$HSO_5^- + e^- \rightarrow SO_4^{2-} + HO^{\cdot} \quad (2)$$

$$HSO_5^- + \text{energy} \rightarrow HO^{\cdot} + SO_4^{\cdot-} \quad (3)$$

$$HSO_5^- + SO_5^{2-} \rightarrow {}^1O_2 + HSO_4^- + SO_4^{2-} \quad (4)$$

$$HSO_5^- - e^- \rightarrow SO_5^{\cdot-} + H^+ \quad (5)$$

$$2SO_5^{\cdot-} \rightarrow {}^1O_2 + S_2O_8^{2-} \quad (6)$$

To date, various catalysts have been developed for PMS activation, such as carbon-based materials, metal-based catalysts, and single-atom catalysts[23-27]. Among these materials, carbon-based materials serve as primary catalysts for PMS activation because of their tunable microenvironments, excellent conductivity, and chemical stability[28]. However, carbon-based materials possess diverse surface-active sites, such as heteroatoms, defects, and functional groups, that originate from the inherently difficult-to-control high-temperature pyrolysis or carbonization processes, thereby severely hampering selective PMS activation[29]. For instance, Deng *et al.* constructed Co-, S-, and O-codoped carbon nitride (CoCN-x) for PMS activation to generate various ROS simultaneously, including radicals (HO$^•$, $SO_4^{•-}$, $O_2^{•-}$) and non-radical species ($^1O_2$, CoO^{2+}, and

electron transfer)[30]. Moreover, Wang *et al.* prepared CoFe encapsulated in N-doped carbon nanotubes (CoFe-N-CNTs) to activate PMS for pollutant degradation. In the CoFe-N-CNTs/PMS system, $^1O_2$, $HO^•$, $SO_4^{•-}$, and $O_2^{•-}$ were detected, and electron transfer and DOTP pathways were also involved[31]. Thus, the rational design of carbon-based catalysts with well-defined and tunable active sites for highly selective ROS generation is critical[32,33]. Indeed, the selectivity of ROS generation is closely related to the electron density of active sites, which determines where oxygen atoms in PMS adsorb and the direction of electron transfer[34,35]. For instance, Zhang *et al.* developed an Fe single-atom catalyst supported on graphitic carbon nitride (Fe_1/CN), with an Fe loading of 11.2 wt% for PMS activation. In Fe_1/CN, the Fe atom in its oxidized state adsorbed the terminal oxygen atom of PMS, efficiently generating $^1O_2$ with 100% selectivity, whereas the electron-rich Fe nanoparticles (NPs) in Fe NP/CN preferentially adsorbed an oxygen atom in the peroxo bond, generating $HO^•$ and $SO_4^{•-}$[36]. Collectively, modulating the electron density of active centers enables selective generation of ROS.

In this study, we constructed a series of Fe-based alloy-doped carbon aerogels (FeM-CA, M = Mo/Co/Ni) as cathodes to electro-activate PMS. The introduced secondary metals were employed to modulate the electron density of Fe, thereby regulating the PMS activation pathways. The morphologies of FeM-CA and the corresponding metal valence states were characterized by electron microscopy and X-ray absorption near-edge structure (XANES), respectively. Electron paramagnetic resonance (EPR) spectroscopy, quenching experiments, and chemical probes were collectively used to qualitatively and quantitatively identify the dominant ROS generated during PMS activation. Furthermore, the mechanisms underlying the different PMS activation pathways of FeM-CA were investigated using *in situ* Raman spectroscopy and temperature-dependent magnetic susceptibility measurements. Additionally, the performance of the FeM-CA/PMS systems was evaluated to assess their matrix tolerance and potential for water treatment. This work provided a theoretical foundation for the rational design of catalysts for PMS activation based on the electronic structure of active sites.

EXPERIMENTAL

Synthesis of FeM-CA

The Fe-based alloy-doped carbon aerogel (denoted as FeM-CA) was synthesized through a previously reported sol-gel method involving solvent exchange and pyrolysis processes[37]. The corresponding chemicals and reagents were listed in the Supplementary Text 1. Firstly, resorcinol, formaldehyde, water and sodium carbonate were thoroughly mixed at a molar ratio of 1:2.1:10.9:0.0008 to obtain a homogeneous solution. Then, a certain amount of metal acetylacetone precursors was gradually added to the solution. The mixture was poured into a rectangular glass mold with the dimensions of 15 cm × 5 cm × 3 cm. The polymerization and aging processes were carried out by maintaining the mold at 30, 50 and 90 °C for 24, 24 and 72 h, respectively. Subsequently, the wet gel was immersed in acetone for 3 days to remove water within the network. The aerogel was air-dried, and then calcined in a tubular furnace at 850 °C for 4 h under a nitrogen flow of 200 mL·min^{-1} with a heating rate of 2.5 °C·min^{-1}. Finally, the obtained carbon aerogel was treated in 1 mol·L^{-1} H_2SO_4 at 80 °C for 8 h to remove unstable metal species. The dimensions of the as-synthesized FeM-CA were 5.0 cm × 2.0 cm × 0.2 cm with a mass of approximately 1.0 g.

Experimental setup

The electrochemical degradation experiments were conducted in a 50-mL cuboidal glass cell, with the as-prepared FeM-CA and Pt foil serving as the cathode and anode, respectively. The direct-current (DC) power supply was set to deliver a constant current of 20 mA during the electrochemical tests. The amperometric i-t measurement was conducted in a three-electrode system, with the as-prepared FeM-CA, Pt foil and Ag/AgCl serving as the working, counter and reference electrodes, respectively. Solutions containing each simulated wastewater contaminant at 10 mg·L^{-1}, including bisphenol A (BPA), benzoic acid (BA), sulfamethoxazole (SMX), tetracycline (TC), and ciprofloxacin (CIP), were treated separately in 40 mL of 4 mM PMS solution. Methanol (100 mM), *tert*-butanol (TBA, 100 mM) and L-histidine (L-His, 5 mM) were used to quench $HO^•$/$SO_4^{•-}$, $HO^•$ and $^1O_2$, respectively. Moreover, BA, nitrobenzene (NB), and furfuryl alcohol (FFA) were selected as probes for $SO_4^{•-}$, $HO^•$, and $^1O_2$, respectively. Notably, separate experiments were conduct-

ed when BA was used as a target pollutant and as a ROS detection probe, respectively. The effects of coexisting ions (5 mM) were evaluated to assess the anti-interference ability of FeM-CA. BPA degradation in actual water samples (Wuquan Mountain spring water, tap water, lake water, snow water, and Yellow River water) was used to investigate the practical applicability of the FeM-CA electrode. Recycling tests were conducted by collecting the used electrode, washing it with deionized water, and drying it in a vacuum oven. All sample aliquots were collected at predetermined intervals and immediately quenched with $Na_2S_2O_3$ to eliminate residual PMS.

RESULTS AND DISCUSSION

Physicochemical characterization of FeM-CA

The integrated FeM-CA electrodes were prepared via a classical sol-gel method [Figure 1A]. The polymerization reaction between resorcinol and formaldehyde under a weakly alkaline environment provided a stable carbon framework for the carbon aerogel. Transition metal NPs promoted the formation of graphitic carbon layers at high temperature, thereby increasing the degree of carbon graphitization and boosting the conductivity of the electrodes. The as-prepared FeM-CA was used as the cathode to electrochemically activate PMS for ROS generation. Subsequently, scanning electron microscopy (SEM) and transmission electron microscopy (TEM) images provided detailed views of all FeM-CA electrodes [Supplementary Text 2]. As illustrated in Figure 1 and Supplementary Figure 1, FeMo-CA, FeCo-CA, and FeNi-CA all exhibited interconnected aerogel network structures in which the alloy NPs were embedded in the carbon layers. The NPs displayed lattice fringes with a spacing of 0.38 nm. For FeMo-CA, the interplanar distance of 0.22 nm was assigned to the (400) planes of the FeMo alloy, and the energy dispersive spectroscopy (EDS) mapping images showed uniform distributions of Fe and Mo [Figure 1B and C]. The lattice-fringe spacings of 0.20 and 0.17 nm observed in Figure 1D and F were attributed to the (011) and (110) facets of the FeCo and FeNi alloys, respectively. The EDS maps of FeCo-CA and FeNi-CA showed that the Fe, Co, and Ni elements were uniformly distributed in the alloy NPs [Figure 1E and 1G]. The contents of metals in FeM-CA were summarized in Supplementary Table 1. Moreover, the X-ray diffraction (XRD) patterns proved that the as-prepared FeM-CA electrodes exhibited well-crystallized alloy diffraction peaks [Supplementary Figure 2], in accordance with the TEM results. The diffraction peaks at 43.7° and 50.9° were assigned to the (101) and (110) planes of the FeNi alloy (PDF#96-901-0018). The prominent peaks at 2θ values of 39.5° and 44.8° corresponded to the (400) plane of FeMo (PDF#96-231-0324) and the (011) plane of FeCo (PDF#96-152-4168), respectively. Accordingly, the Brunauer-Emmett-Teller (BET) surface areas of FeMo-CA, FeNi-CA, and FeCo-CA were 536.8992, 666.3775, and 647.6627 $m^2 \cdot g^{-1}$, respectively [Supplementary Figure 3]. Moreover, all isotherms were classified as Type II isotherms, indicating the coexistence of mesopores and macropores in these carbon aerogels. This result suggested that the introduction of different secondary metals significantly regulated the surface area of the carbon aerogels, consequently affecting the effective contact area between active sites and PMS.

The chemical state and coordination environment of metal species in FeM-CA were investigated using XANES at the atomic level. The Fe K-edge XANES profiles of FeM-CA were similar to those of Fe foil but differed from those of the iron oxides [Figure 2A]. To quantitatively analyze the above absorption-edge shifts, valence-state fitting was carried out on the Fe K-edge XANES data. The average valence states of Fe in all FeM-CA electrodes were close to zero [Figure 2B], indicating that Fe was predominantly present as metallic alloy NPs rather than oxides or single-atom sites. Accordingly, the valence states of Ni and Co were fitted to zero, indicating strong electronic hybridization between Fe and Co/Ni and the formation of an alloy phase [Supplementary Figures 4 and 5]. In stark contrast, Mo exhibited a distinctly positive valence of +1.89, indicating electron transfer between Fe and Mo [Supplementary Figure 6]. Subsequently, Fourier--transform k3-weighted extended X-ray absorption fine structure (FT-EXAFS) analysis was performed to investigate the local coordination environment of Fe species in FeM-CA. As shown in Figure 2C, the characteristic peak at 2.2 Å was attributed to the Fe–Fe coordination. Similarly, the dominant M–M peaks were observed in the FT-EXAFS spectra collected at the Mo, Co, and Ni K-edges [Figure 2D-F], consistent with the K-edge XANES results described above. Notably, compared with pure metal foils,

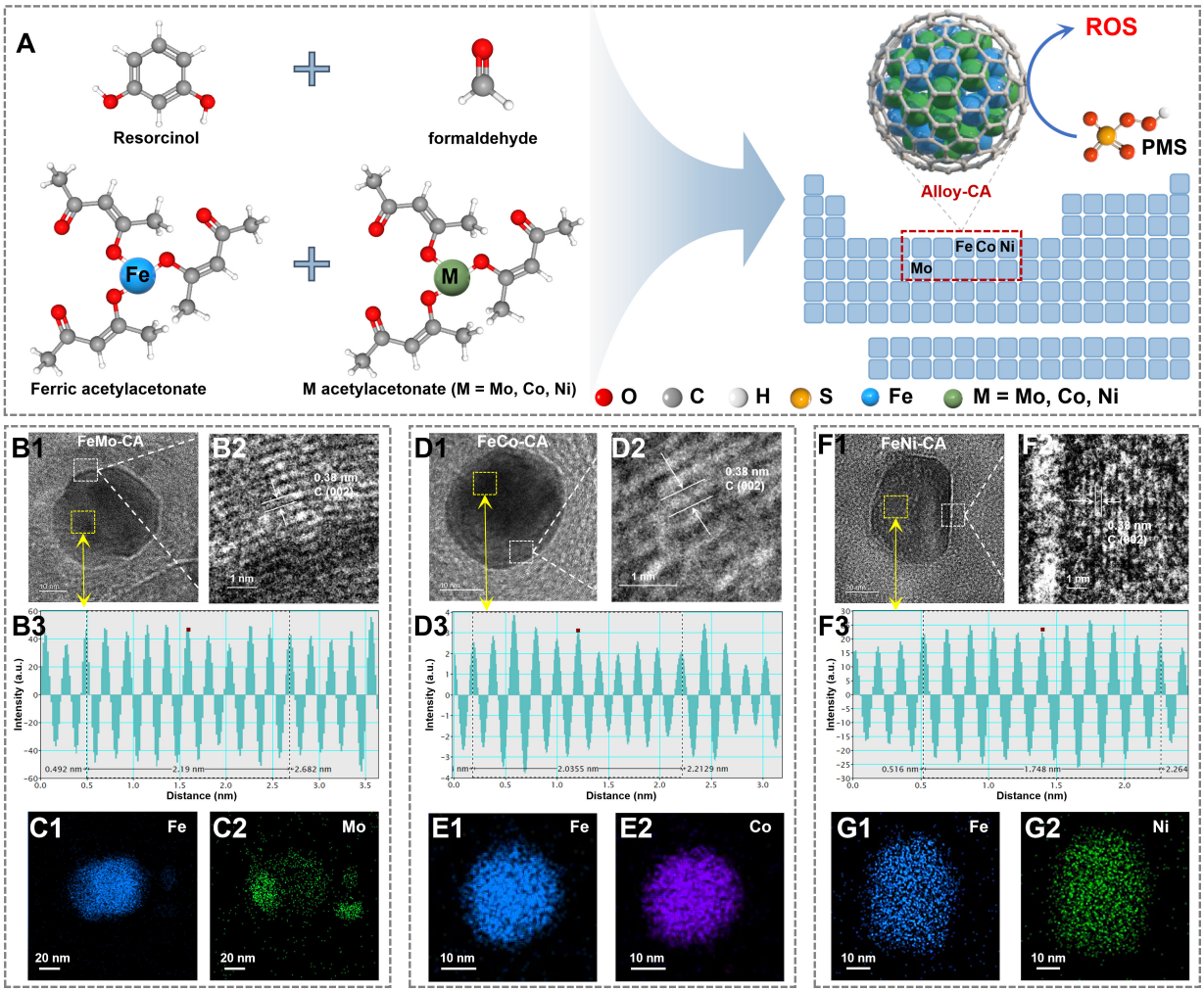


Figure 1. (A) Schematic illustration of the preparation of the FeM-CA electrode; (B1) TEM images; (B2) lattice fringe of carbon; (B3) Intensity line profile; and (C1 and C2) EDS maps of FeMo-CA; (D1) TEM images; (D2) lattice fringe of carbon; (D3) Intensity line profile; and (E1 and E2) EDS maps of FeCo-CA; (F1) TEM images; (F2) lattice fringe of carbon; (F3) Intensity line profile; and (G1 and G2) EDS maps of FeNi-CA. ROS: Reactive oxygen species; PMS: peroxymonosulfate; CA: carbon aerogel; TEM: transmission electron microscopy; EDS: energy dispersive spectroscopy.

these M–M peaks exhibited slight shifts in their *R* values, which were attributable to interactions between Fe and the secondary metals (Co, Ni, and Mo). The wavelet-transform analysis of the k^2-weighted EXAFS spectra was used to further confirm the Fe coordination structure in FeM-CA. As expected, the maximum intensity at $k \approx 8$ Å^{-1} corresponded to Fe–Fe coordination [Figure 2G and Supplementary Figure 7]. In addition, the corresponding wavelet-transform EXAFS (WT-EXAFS) spectra at the Co, Mo, and Ni K-edges collectively confirmed the alloy structures in FeMo-CA, FeCo-CA, and FeNi-CA [Supplementary Figures 8-10].

Identification and quantitation of ROS in FeM-CA/PMS system

EPR was employed to identify ROS generated in FeM-CA/PMS systems using 5,5-dimethyl-1-pyrroline-N-oxide (DMPO) and 2,2,6,6-tetramethyl-4-piperidinol (TEMP) as spin-trapping agents [Supplementary Text 3]. Clearly, only a typical triplet signal of the TEMP-$^1O_2$ adduct (1:1:1; hyperfine coupling constants $A_N = A_H = 1.7$ mT) was detected in the FeNi-CA/PMS system [Figure 3A and B]. Additionally, a remarkable DMPO-$SO_4^{\bullet-}$ adduct signal (hyperfine coupling constants $A_N = 1.3$ mT, $A_H = 0.9$ mT, $A_H = 1.5$ mT and $A_H = 0.08$ mT) was observed in FeMo-CA/PMS system, while the weak TEMP-$^1O_2$ signal was attributed to the sluggish self-decomposition of PMS[38]. These results indicated that $^1O_2$ and $SO_4^{\bullet-}$ were selectively generated by FeNi-CA and FeMo-CA, respectively. In the FeCo-CA/PMS system, a strong four-line spectrum

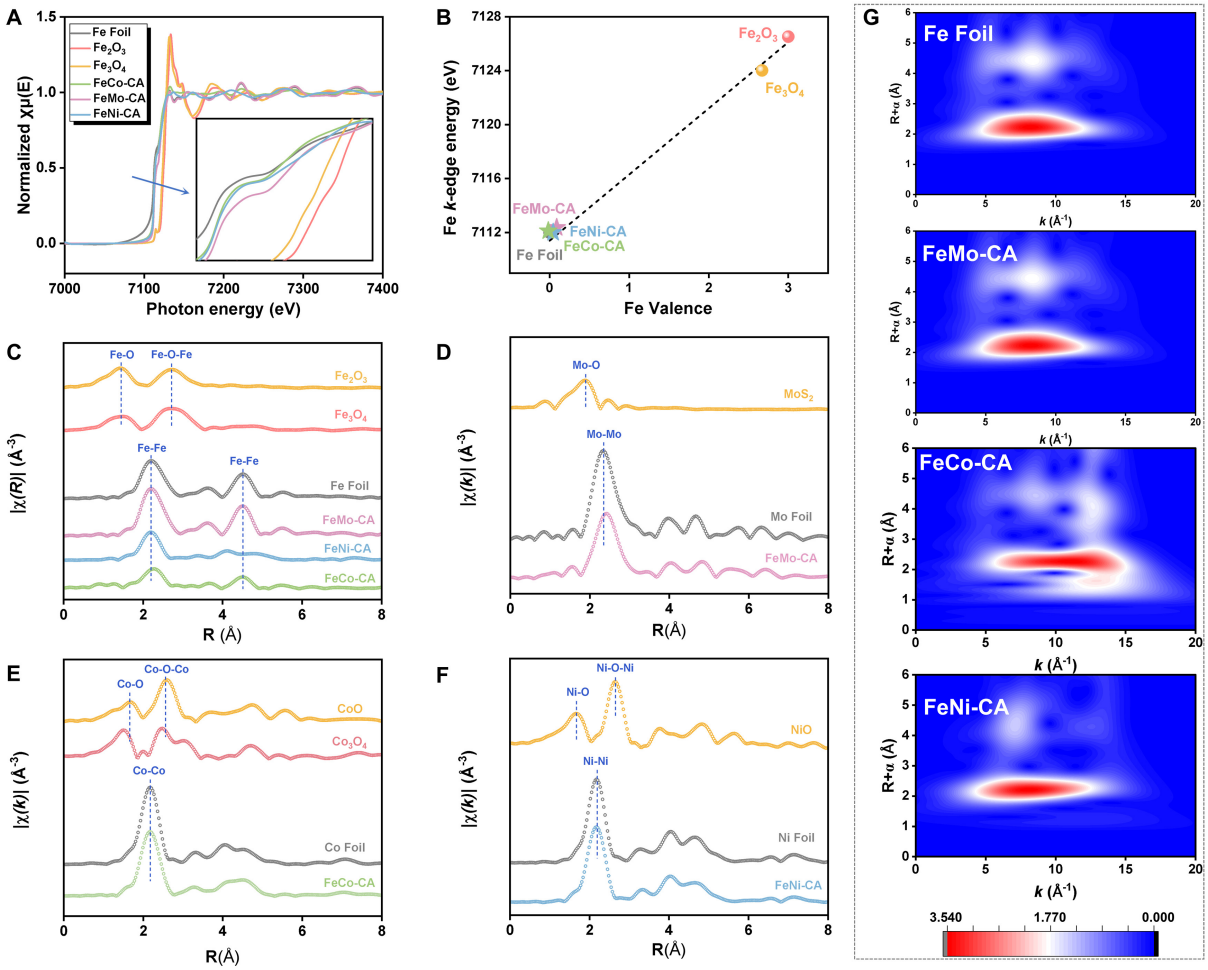


Figure 2. (A) Fe K-edge XANES spectra, (B) valence states and (C) FT-EXAFS spectra at the Fe K-edge in R space for FeCo-CA, FeMo-CA, FeNi-CA, standard Fe foil, Fe_2O_3 and Fe_3O_4; FT-EXAFS spectra in R space at the (D) Mo K-edge for FeMo-CA, (E) Co K-edge for FeCo-CA, and (F) Ni K-edge for FeNi-CA; (G) The wavelet-transform analysis of the k^2-weighted EXAFS spectra at the Fe K-edge for Fe foil, FeMo-CA, FeCo-CA, and FeNi-CA. XANES: X-ray absorption near-edge structure; FT-EXAFS: Fourier-transform k3-weighted extended X-ray absorption fine structure.

induced by $HO^•$ (1:2:2:1; hyperfine coupling constants $A_N = A_H = 1.5$ mT), together with a DMPO-$SO_4^{•-}$ signal and a TEMP-$^1O_2$ signal, demonstrated that $HO^•$, $SO_4^{•-}$, and $^1O_2$ were generated simultaneously. To further verify the main ROS in FeMo-CA/PMS systems, methanol, L-His, and TBA were used as the scavengers for $HO^•$/$SO_4^{•-}$, $^1O_2$, and $HO^•$, respectively[39]. TBA was employed as a selective scavenger for $HO^•$ because its second-order reaction rate constant of TBA with $HO^•$ ($k = 3.8 \times 10^8$ M^{-1} s^{-1}) was several orders of magnitude higher than that with $SO_4^{•-}$ ($k = 4 \times 10^5$ M^{-1} s^{-1}). Methanol acts as a universal radical scavenger because it reacts rapidly with $HO^•$ ($k = 9.7 \times 10^8$ M^{-1} s^{-1}) and $SO_4^{•-}$ ($k = 3.2 \times 10^7$ M^{-1} s^{-1})[40]. Notably, the $SO_4^{•-}$ and $^1O_2$ signals disappeared after methanol and L-His were added, further confirming that $SO_4^{•-}$ and $^1O_2$ were the dominant ROS in the FeMo-CA/PMS and FeNi-CA/PMS systems, respectively [Figure 3C and D]. Moreover, the intensities of the $HO^•$, $SO_4^{•-}$ and $^1O_2$ signals decreased in the presence of TBA, methanol, and L-His, providing strong evidence for the coexistence of diverse ROS in the FeCo-CA/PMS system [Figure 3E and F]. Subsequently, BA, FFA, and NB were selected as probes to quantify the steady-state concentrations ($[ROS]_{ss}$) of $SO_4^{•-}$, $^1O_2$, and $HO^•$, respectively [Figure 3G, Supplementary Text 4 and Supplementary Table 2]. As shown in Figure 3H, the measured $[^1O_2]_{ss}$ in the FeNi-CA/PMS reached 1.99 × 10^{-11} M, which was higher than that in the FeCo-CA/PMS system (1.32 × 10^{-11} M) and pure PMS (6.50 × 10^{-12} M) systems. Meanwhile, the obtained $[SO_4^{•-}]_{ss}$

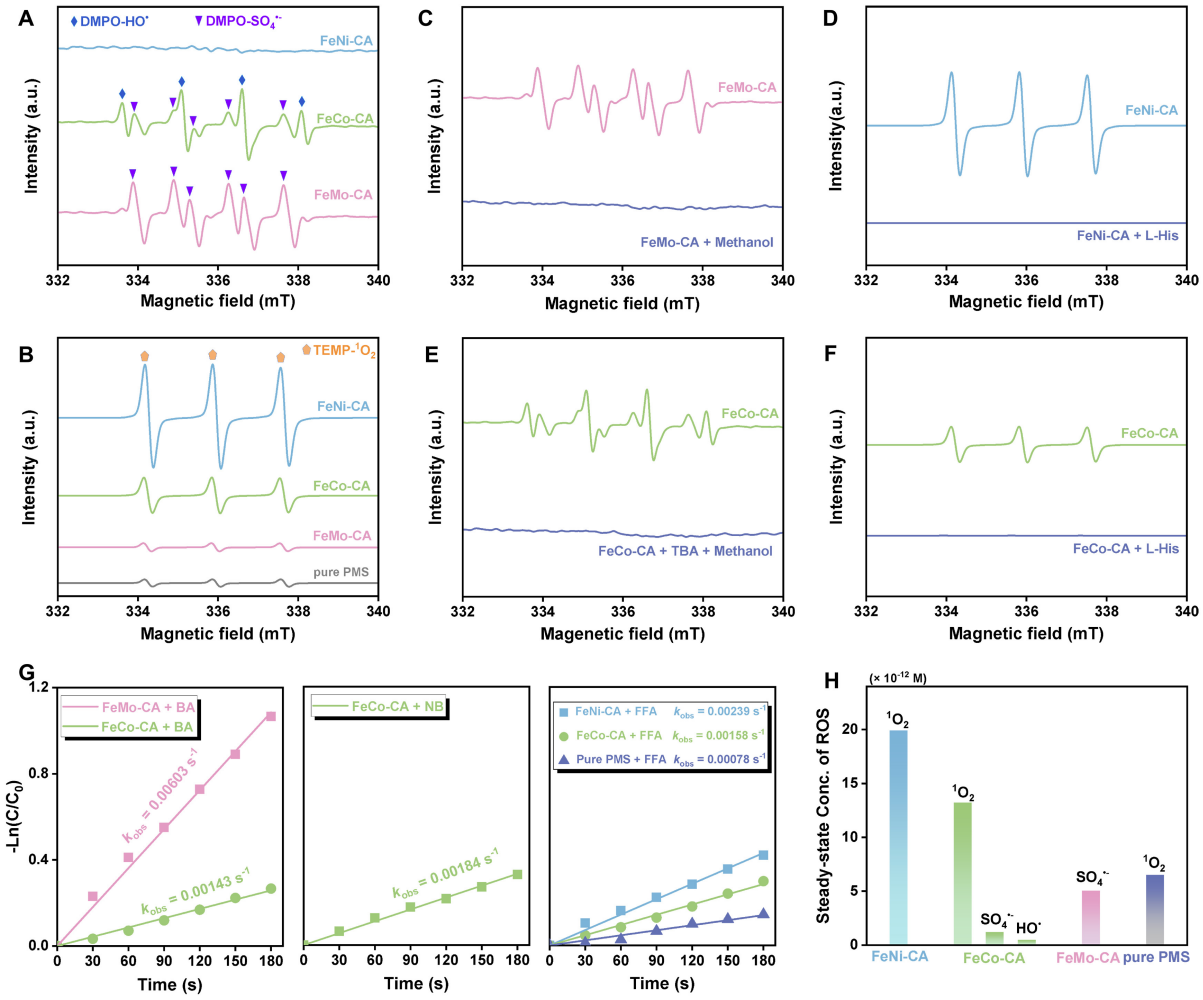


Figure 3. EPR spectra of the FeCo-CA, FeMo-CA, and FeNi-CA using (A) DMPO and (B) TEMP as spin-trapping agents; Quenching experiments for (C) FeMo-CA, (D) FeNi-CA, and (E and F) FeCo-CA; (G) Pseudo-first-order kinetic constants (k_{obs}) of the selected probe compounds and (H) steady-state concentrations of ROS in the FeCo-CA/PMS, FeMo-CA/PMS, FeNi-CA/PMS, and pure PMS systems. DMPO: 5,5-dimethyl-1-pyrroline-N-oxide; CA: carbon aerogel; L-His: L-histidine; TEMP: 2,2,6,6-tetramethyl-4-piperidinol; PMS: peroxymonosulfate; TBA: *tert*-butanol; BA: benzoic acid; NB: nitrobenzene; FFA: furfuryl alcohol; EPR: electron paramagnetic resonance; ROS: reactive oxygen species.

in the FeMo-CA/PMS system (5.03×10^{-12} M) was 4.2-fold higher than that in the FeCo-CA/PMS (1.19×10^{-12} M) system. Moreover, the $[HO^{\bullet}]_{ss}$ in the FeCo-CA/PMS system was 4.72×10^{-13} M, which was lower than the concentrations of the other ROS. Taken together, the FeNi-CA and FeMo-CA selectively activated PMS via non-radical ($^1O_2$) and radical pathways ($SO_4^{\bullet-}$), respectively, while the FeCo-CA enabled the simultaneous generation of multiple ROS ($SO_4^{\bullet-}$, $HO^{\bullet}$, and $^1O_2$).

Mechanistic insights into PMS activation over FeM-CA cathodes

To clarify the role of the carbon layer in PMS activation, *in situ* Raman spectroscopy was used to monitor the dynamic evolution of the carbon-framework microstructure within FeM-CA. As illustrated in Supplementary Figure 11, the characteristic signals of D (~1,350 cm^{-1}) and G (1,580 cm^{-1}) bands were observed in all FeM-CA electrodes and were assigned to the sp^3-related defects in carbon and sp^2-hybridized graphitic carbon, respectively. The I_D/I_G values followed the order: FeMo-CA (0.94) < FeCo-CA (1.03) < FeNi-CA (1.14), indicating that FeNi-CA possessed the most abundant defects, while FeMo-CA exhibited the highest degree of graphitization. After PMS was added, no significant shifts in the D and G bands were observed in any of the FeM-CA electrodes, and the I_D/I_G ratios remained stable over the 0-300 s reaction period, suggesting

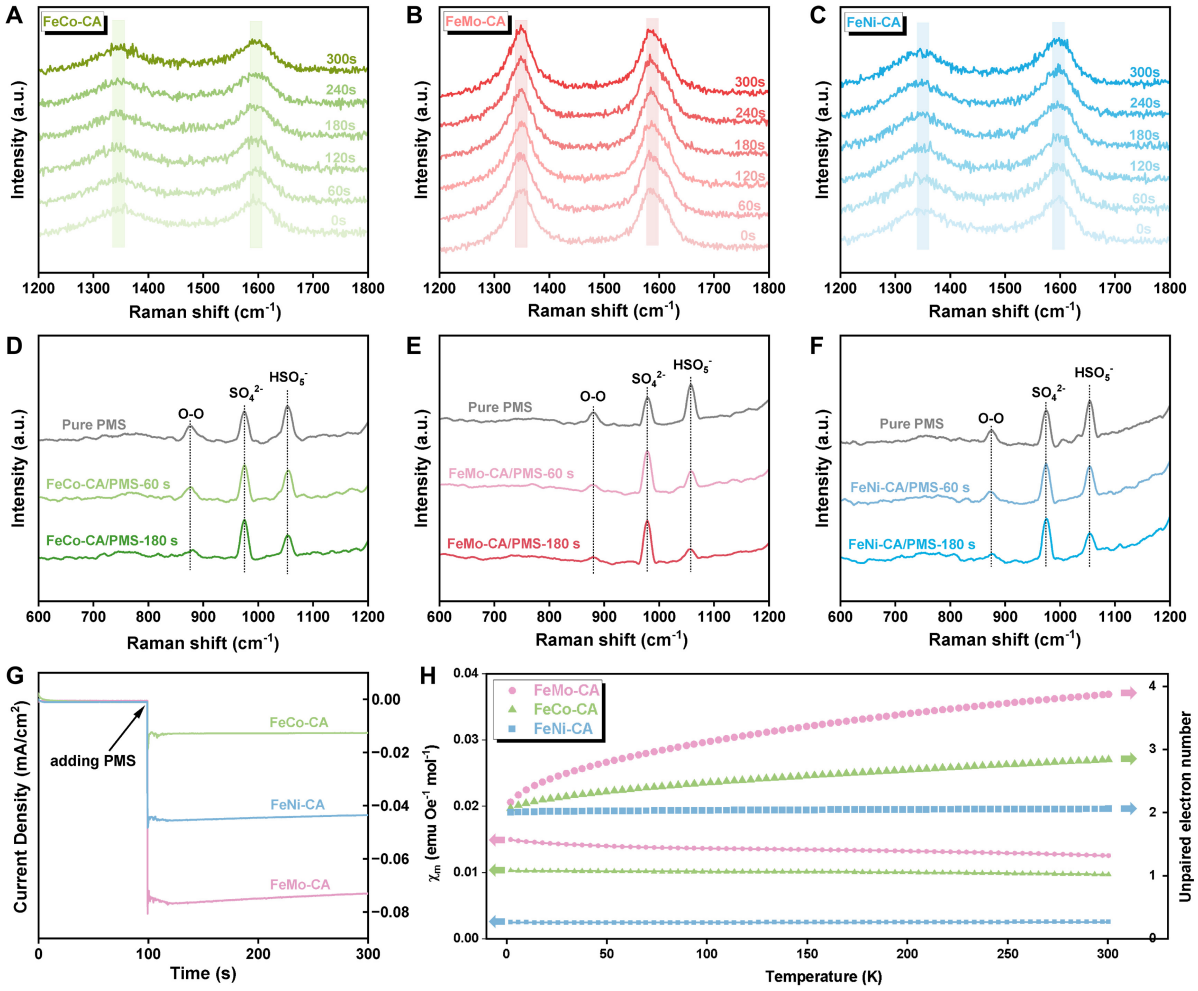


Figure 4. *In situ* Raman spectra of (A) FeCo-CA, (B) FeMo-CA, and (C) FeNi-CA during PMS activation at different reaction times; *In situ* Raman spectra of (D) FeCo-CA/PMS, (E) FeMo-CA/PMS, and (F) FeNi-CA/PMS systems at reaction times of 60 and 180 s; (G) Amperometric i-t curves of FeCo-CA, FeMo-CA, and FeNi-CA after PMS addition; (H) χ_m-T curves and the calculated numbers of unpaired electrons in the d orbitals of FeCo-CA, FeMo-CA, and FeNi-CA. PMS: Peroxymonosulfate; CA: carbon aerogel.

that the carbon structure remained stable during the reaction. These findings confirmed that the carbon skeletons were not involved in PMS activation [Figure 4A-C]. The slight increases in the intensities of the D and G bands mainly arose from the interfacial electronic response. Subsequently, PMS evolution on the surface of the FeM-CA cathodes was investigated. As illustrated in Figure 4D-F, three characteristic peaks were observed in the spectrum of pure PMS. The peaks at 880 and 1,060 cm^{-1} were assigned to the stretching vibrations of the O–O bond and SO_3^- group of PMS (HSO_5^-), respectively, whereas the peak at 980 cm^{-1} was attributed to the symmetric stretching vibration of the S=O bond in SO_4^{2-}. Notably, the intensities of the peaks assigned to the O–O bond and SO_3^- group decreased sharply, whereas the intensity of the S=O band increased, indicating that PMS was efficiently decomposed in all FeM-CA electrodes. In addition, a red shift of the SO_3^- peak occurred in the FeMo-CA/PMS system, resulting in an increase in electron-cloud density in SO_3^- and a decrease in the S–O bond order [Supplementary Figure 12A]. This result indicated that the FeMo alloy tended to transfer electrons to PMS, promoting O–O bond cleavage and the generation of $SO_4^{\bullet-}$ radicals[41]. In contrast, the blue shift of the SO_3^- peak in the FeNi-CA/PMS system was attributed to a decrease in electron cloud density and an increase in S–O bond polarity, suggesting that the FeNi alloy tended to withdraw electrons from PMS, thereby facilitating $^1O_2$ generation via a non-radical pathway [Supplementary Figure 12B]. As shown in Supplementary Figure 12C, the preferential blue shift in the FeCo-CA/PMS system was attributed to the higher

steady-state concentration of non-radical $^1O_2$ than that of the radicals ($SO_4^{\bullet-}$ and $HO^{\bullet}$) shown in Figure 3H. These observations were consistent with the aforementioned identification and quantitative analysis of ROS, providing evidence for the distinct PMS activation mechanisms of the three FeM-CA electrodes.

Subsequently, to elucidate the mechanism of PMS activation from an electrochemical perspective, amperometric i-t curves were recorded for FeCo-CA, FeMo-CA, and FeNi-CA to monitor the current responses after PMS injection [Figure 4G]. Specifically, FeMo-CA exhibited a cathodic current response of -0.073 mA·cm^{-2} after adding PMS, which was 1.7- and 5.2-fold greater in magnitude than the responses for FeNi-CA (-0.043 mA·cm^{-2}) and FeCo-CA (-0.014 mA·cm^{-2}), respectively. A more negative current indicated faster electron transfer from the electrode to PMS. In other words, FeMo-CA, which possessed more available electrons, could rapidly transfer electrons to PMS, thereby generating $SO_4^{\bullet-}$ via a radical pathway. Conversely, electron-deficient FeNi-CA displayed a tendency to accept electrons from PMS, thereby producing $^1O_2$ via a non-radical route. These observations were highly consistent with the above *in situ* Raman and EPR results.

In theory, the selectivity of ROS generation was related to the electronic structure of active sites. Therefore, temperature-dependent magnetic susceptibility [molar magnetic susceptibility multiplied by temperature (χmT)] was measured to calculate the effective magnetic moment and the average number of unpaired electrons in three FeM-CA electrodes[42]. As depicted in Figure 4H, the numbers of unpaired electrons in FeMo-CA, FeCo-CA, and FeNi-CA were 3.87, 2.84, and 2.05, respectively. The number of unpaired electrons in the three FeM-CA electrodes was closely related to the d-electron count of the secondary metal. As the d-electron count of the secondary metal increased from Mo ($4d^5 5s^1$) to Co ($3d^7 4s^2$) and Ni ($3d^8 4s^2$), the d-band filling of the alloy gradually rose. The 4d orbitals of Mo exhibited greater spatial extension than the 3d orbitals of Co and Ni. Hybridization between Fe 3d and Mo 4d induced prominent d-band splitting and spin-state reconstruction. The FeMo alloy had the highest number of unpaired electrons among the three samples and acted as a potent electron donor to PMS, thereby driving the radical pathway. However, Ni possesses the largest number of 3d valence electrons. The FeNi alloy showed the highest d-band filling of the three samples, where a large fraction of spin orbitals is filled by paired electrons. Thus, FeNi-CA, which had the fewest unpaired electrons, activated PMS through a non-radical pathway dominated by $^1O_2$. Furthermore, Co has more 3d electrons than Fe. The FeCo alloy featured a higher d-band filling level than FeMo, with more spin-up orbitals occupied and a lower population of unpaired electrons. Therefore, FeCo-CA, which had an intermediate number of unpaired electrons, exhibited both radical and non-radical pathways. These findings further demonstrated that selective ROS generation was closely linked to the electronic structure of active sites.

Application potential of FeM-CA/PMS for water purification

Several parameters were used to comprehensively evaluate the application potential of FeM-CA for water treatment, including degradation kinetics, factors affecting performance, and recyclability. BPA, a typical EC with endocrine-disrupting activity, was selected as a model pollutant to assess the electrochemical performance of the as-prepared FeM-CA electrodes for PMS activation [Supplementary Text 3]. As illustrated in Figure 5A, the FeCo-CA/PMS system achieved approximately 100% BPA degradation within 150 s, exceeding the degradation achieved by the FeNi-CA/PMS (~89%) and FeMo-CA/PMS (~60%) systems. The corresponding pseudo-first-order kinetic constant (k_{obs}) followed the order: FeMo-CA/PMS (0.006 s^{-1}) < FeNi-CA/PMS (0.015 s^{-1}) < FeCo-CA/PMS (0.027 s^{-1}) (Figure 5B). The lower degradation rate in the FeMo-CA/PMS system was attributed to the lower steady-state concentration of $SO_4^{\bullet-}$. Moreover, the total organic carbon (TOC) removal efficiency in the FeCo-CA/PMS system (95.2%) was higher than the efficiencies in the FeNi-CA/PMS (64.7%) and FeMo-CA/PMS (31.3%) systems (Figure 5C). Accordingly, FeCo-CA exhibited excellent degradation and mineralization performance in water treatment, benefiting from the synergistic dual-pathway mechanism involving both radical and non-radical ROS. In addition, various ECs were further used to explore the broad-spectrum applicability of FeCo-CA/PMS system, including SMX, TC, CIP and BA. As depicted

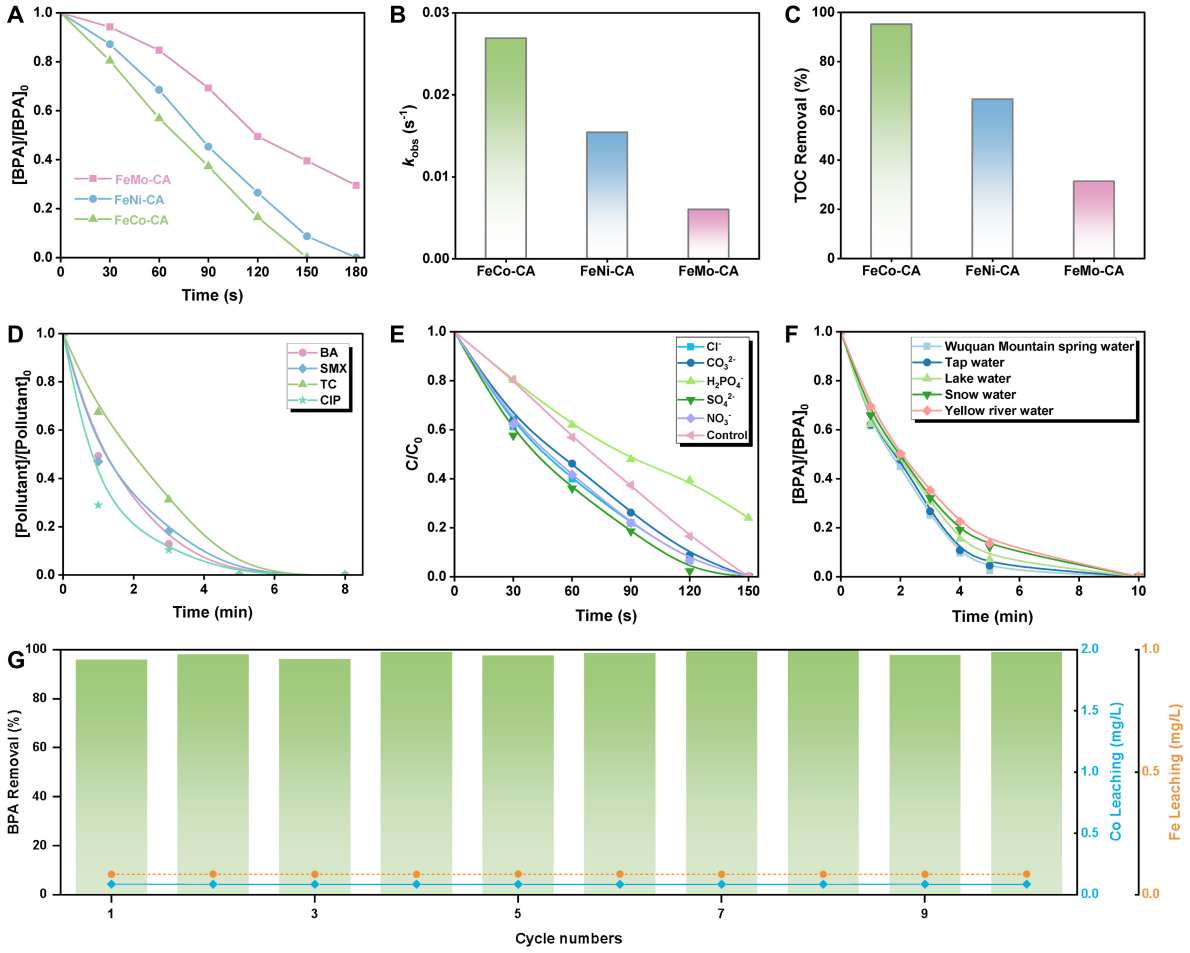


Figure 5. (A) BPA degradation performance, (B) the corresponding pseudo-first-order kinetic constants (k_{obs}) and (C) TOC removal efficiency in the FeCo-CA/PMS, FeMo-CA/PMS, and FeNi-CA/PMS systems; (D) Degradation performance of various pollutants, (E) effects of coexisting anions, and (F) effects of water matrices on BPA degradation in the FeCo-CA/PMS system; (G) Cycling performance of BPA degradation and metal leaching in the FeCo-CA/PMS system. Reaction conditions: [Current] = 20 mA, [PMS] = 4 mM, $[BPA]_0$ = $[BA]_0$ = $[SMX]_0$ = $[TC]_0$ = $[CIP]_0$ = 10 mg·L^{-1}, $[anions]_0$ = 5 mM. TOC: Total organic carbon; BA: benzoic acid; SMX: sulfamethoxazole; TC: tetracycline; CIP: ciprofloxacin; BPA: bisphenol A; PMS: peroxymonosulfate; CA: carbon aerogel.

in Figure 5D, complete removal of various ECs was achieved within 8 min. Differences in degradation among pollutants were probably attributable to the electron-donating or electron-withdrawing properties of their substituent groups. Furthermore, the effects of coexisting anions and water matrices on BPA degradation were investigated to assess the practical applicability of the FeCo-CA/PMS system. As expected, the most common anions clearly promoted BPA removal in the FeCo-CA/PMS system, including Cl^-, CO_3^{2-}, SO_4^{2-} and NO_3^-. This effect was attributed to the high steady-state concentration of $^1O_2$, indicating the system's superior anti-interference capability (Figure 5E). Moreover, the introduced ions enhanced the electrical conductivity of the solution, consequently accelerating the degradation kinetics of BPA. However, the BPA degradation efficiency decreased from 100% to 76% in the presence of $H_2PO_4^-$ because $H_2PO_4^-$ strongly quenches radicals ($HO^•$ and $SO_4^{•-}$)[43]. In addition, water samples with complex matrices were used to assess the environmental adaptability of the FeCo-CA/PMS system, including Wuquan Mountain spring water, tap water, lake water, snow water, and Yellow River water. As shown in Figure 5F, BPA removal reached 100% in the different natural water samples within 10 min, although this was slower than in deionized water (150 s). This difference was attributed to coexisting organic and inorganic substances that quenched the radicals. Furthermore, the FeCo-CA/PMS system maintained BPA removal efficiencies of 95%–100% over 10 cycles, with negligi-

ble leaching of Fe and Co from the cathodes (< 0.1 mg L^{-1}). No obvious differences were observed between the XRD patterns of fresh and used FeCo-CA [Supplementary Figure 13]. These results collectively demonstrated the excellent stability of FeCo-CA in water purification. Taken together, the FeCo-CA/PMS system retained high removal efficiency in complex water matrices, highlighting its anti-interference capability and potential for practical water remediation.

CONCLUSIONS

In this work, Fe-based alloy-doped carbon aerogels (FeM-CA, M = Mo/Co/Ni), prepared via a typical sol-gel method, were used as cathodes to electro-activate PMS for ROS generation. SEM and TEM images, together with EDS maps, showed interconnected network structures in which alloy NPs were encapsulated by the carbon aerogel. XANES profiles demonstrated that the average valence states of Fe in all FeM-CA electrodes were close to 0. Accordingly, the valence states of Ni, Co and Mo were 0, 0, and +1.89, respectively, indicating the electronic hybridization between Fe and Co/Ni/Mo and the formation of an alloy phase. EPR and quenching experiments indicated that $SO_4^{\bullet-}$ and $^1O_2$ were the dominant ROS in the FeMo-CA/PMS and FeNi-CA/PMS systems, respectively, while $HO^{\bullet}$, $SO_4^{\bullet-}$ and $^1O_2$ coexisted in the FeCo-CA/PMS system. Furthermore, temperature-dependent magnetic susceptibility measurements combined with *in situ* Raman spectroscopy indicated that the introduction of secondary metals (Mo, Co, and Ni) modulated the electron density of Fe, thereby regulating the PMS activation pathways. Specifically, the electron-rich FeMo-CA, with abundant unpaired electrons, facilitated the cleavage of the O–O bond in PMS to selectively generate $SO_4^{\bullet-}$. In contrast, the electron-deficient FeNi-CA, which had fewer unpaired electrons, tended to accept electrons from PMS, thereby inducing a non-radical pathway dominated by $^1O_2$. FeCo-CA, which had an intermediate number of unpaired electrons, exhibited both radical and non-radical pathways, resulting in the simultaneous generation of multiple ROS ($HO^{\bullet}$, $SO_4^{\bullet-}$, and $^1O_2$). Moreover, the FeCo-CA/PMS system showed superior performance in pollutant degradation, matrix tolerance, and long-term stability, highlighting its potential for practical water remediation. This work provided a novel strategy and a theoretical basis for the precise regulation of ROS generation in PMS-AOP systems.

DECLARATIONS

Authors' contributions

Conceptualization, data curation, formal analysis, visualization, and writing - original draft: Chen, M.

Data curation, methodology, validation, formal analysis, investigation, visualization, and writing - original draft: Dou, Y.

Formal analysis: Liu, X.; Li, Y.

Conceptualization, supervision, project administration, funding acquisition, and writing - review & editing: Zhao, H.

Availability of data and materials

All data required to support the conclusions of this paper are included in the manuscript and the Supplementary Materials. Additional data related to this paper can be obtained from the corresponding author upon request.

AI and AI-assisted tools statement

Not applicable.

Financial support and sponsorship

This work was supported by the National Natural Science Foundation of China (Project Nos. 22476152 and 22122606) and the National Key R&D Program of China (No. 2024YFA1211002).

Conflicts of interest

Zhao, H. is an Editorial Board Member of *Greenverse Science*. She was not involved in any aspect of the editorial process, including reviewer selection, manuscript handling, or decision-making. The other authors declare that there are no conflicts of interest.

Ethical approval and consent to participate

Not applicable.

Consent for publication

Not applicable.

Copyright

© The Author(s) 2026.

Supplementary Materials

Supplementary Materials

REFERENCES

1. Cui, H. L.; Gao, S. H.; Wang, H. C.; et al. Big data integration for environmental risk assessment of emerging contaminants. *Nat. Sustain.* **2026**, *9*, 196-206. DOI
2. Liu, T.; Zhang, Y.; Shan, Z.; et al. Covalent organic framework membrane for efficient removal of emerging trace organic contaminants from water. *Nat. Water.* **2023**, *1*, 1059-67. DOI
3. Wang, S.; Dong, H.; Shao, B.; et al. High-valent iron species (Fe(IV)/Fe(V)) for selective oxidation of emerging contaminants: mechanisms, applications, and future directions. *Environ. Sci. Technol.* **2025**, *59*, 23005-23. DOI PubMed
4. Su, W.; Liu, W.; Wu, H.; et al. Chlorination-properties-performance of polyamide nanofiltration membranes for the rejection of emerging contaminants. *Water. Res.* **2025**, *284*, 124030. DOI PubMed
5. Chen, Y.; Li, Q.; Su, R.; et al. Oxygen vacancies-mediated the peracetic acid activation to selectively generate $^1O_2$ for water decontamination. *Water. Res.* **2025**, *282*, 123765. DOI PubMed
6. Hao, Y.; Zhang, Y.; Wang, J.; Zhang, H.; Sun, L.; Cui, M. Micro-nanobubbles-assisted advanced oxidation processes and their inactivation effect on Gymnodinium catenatum: O_3/H_2O_2/UV multi-oxidant system. *Chem. Eng. J.* **2025**, *520*, 166123. DOI
7. Marino, L.; Gagliano, E.; Santoro, D.; Roccaro, P. Fluorescence sensor enabled control of contaminants of emerging concern in reclaimed wastewater using ozone-based treatment processes. *Water. Res.* **2025**, *268*, 122616. DOI PubMed
8. Tong, Y.; Wang, X.; Zhang, Y.; Xu, J.; Sun, C. Reactive species in peracetic acid-based AOPs: a critical review of their formation mechanisms, identification methods and oxidation performances. *Water. Res.* **2025**, *272*, 122917. DOI PubMed
9. Wang, W. M.; Wang, W. L.; Gan, L.; et al. Self-replenishing neutral Fenton-like treatment for emerging contaminants through single Fe atom electron configuration regulation. *Water. Res.* **2025**, *276*, 123251. DOI PubMed
10. Zhang, X.; Wang, Z.; Hu, J. Performance comparison of O_3 and O_3/Peroxymonosulfate (PMS) advanced oxidation processes for the antibiotics removal in wastewater treatment. *J. Hazard. Mater.* **2025**, *496*, 139248. DOI PubMed
11. Chen, H.; Yin, R.; Zhu, M. How to enhance persulfate processes by external-field effects: from fundamentals to applications. *Water. Res.* **2025**, *274*, 123026. DOI PubMed
12. Li, N.; Ye, J.; Dai, H.; et al. A critical review on correlating active sites, oxidative species and degradation routes with persulfate-based antibiotics oxidation. *Water. Res.* **2023**, *235*, 119926. DOI PubMed
13. Wu, Y.; Huang, D.; Li, D.; Qian, X.; Niu, J. From ambiguity to application: deciphering non-radical pathways in heterogeneous persulfate activation. *Adv. Mater.* **2026**, *38*, e16166. DOI PubMed
14. Chen, Z.; Wang, J.; Yang, B.; et al. Organic carbon transfer process in advanced oxidation systems for water clean-up. *Nat. Water.* **2025**, *3*, 334-44. DOI
15. Li, Z.; Ji, X.; Li, Q.; et al. Asymmetric coordination engineering of MXene-based metal arrays for oriented generation of high-valent metal-oxo species from peroxymonosulfate for fast water decontamination. *Angew. Chem. Int. Ed.* **2026**, *65*, e22714. DOI PubMed
16. Zhang, Y. J.; Huang, G. X.; Winter, L. R.; et al. Simultaneous nanocatalytic surface activation of pollutants and oxidants for highly efficient water decontamination. *Nat. Commun.* **2022**, *13*, 3005. DOI PubMed PMC
17. Wang, Z.; Zuo, Q.; Deng, F.; et al. Beyond passive degradation: pre-adsorbed pollutants as electronic modulators for enhanced PMS activation on single-atom iron sites. *Appl. Catal. B:. Environ. Energy.* **2026**, *392*, 126725. DOI
18. Liu, Y.; Zhang, G.; He, T.; et al. Planar-axial synergistic modulation of Fe_{SA}-O/P-NC single-atom catalyst for high-efficiency PMS activation in sulfonamides degradation. *Appl. Catal. B:. Environ. Energy.* **2026**, *382*, 125967. DOI
19. Yao, X.; Li, R.; Shen, L.; Zhao, L.; Lin, H. A novel magnetically induced Co@NC-modified electrochemical membrane for continuous peroxymonosulfate activation: achieving ultrafast and cost-effective purification with elucidation of mechanism and application potential. *Water. Res.* **2025**, *287*, 124436. DOI PubMed
20. Yuan, K.; Chen, D.; Ma, S.; et al. Breaking the Schottky barrier by strain effect: N-doped zero-valent iron for dual-pathway synergistic peroxymonosulfate activation. *Adv. Funct. Mater.* **2026**. , 36, e28553. DOI
21. Jing, J.; Wu, H.; Wang, X.; et al. Anode-cathode synergistic filter activating peroxymonosulfate at multiple active sites for highly efficient and economical water purification. *Environ. Sci. Technol.* **2025**, *59*, 11919-34. DOI PubMed
22. Liu, J.; Sun, Z.; Wu, Z.; Shi, J.; Dong, G.; Deng, H. Cu, N co-regulation of Fe sites steers PMS oxidation toward a matrix-tolerant nonradical pathway via local symmetry perturbation and interfacial electron transfer. *Chem. Eng. J.* **2026**, *550*, 182787. DOI
23. Kang, H.; Chen, Y.; Cheng, M.; et al. State-of-the-art structural regulation methods and quantum chemistry for carbon-based single-atom catalysts in advanced oxidation process: critical perspectives into molecular level. *Adv. Mater.* **2025**, *37*, 2505128. DOI PubMed
24. Li, N.; Hao, Y.; Liang, L.; et al. A critical review on persulfate-based catalytic systems: deactivation mechanisms and regulation strategies. *Water. Res.* **2026**, *302*, 126193. DOI PubMed
25. Liu, Y.; Zhou, A.; Duan, C.; Tian, J.; Wang, J. Dynamic structural evolution of carbon catalysts during persulfate activation rewires nonradical pathways for water decontamination. *Water. Res.* **2026**, *301*, 126100. DOI PubMed

26. Yu, G.; Zhang, J.; Wei, H.; Zhao, W.; Zhu, M. Tailored Ni-O-Ni dimers drive radical/non-radical pathways in peroxymonosulfate oxidation processes to remove emerging contaminants. *Sci. China. Chem.* **2026**, *69*, 1548-57. DOI
27. Ye, F.; Wang, J. R.; Ding, Y.; et al. Photoswitching-modulated interfacial electron transfer in single-atom Co-TiO_2 for enhanced pollutant mineralization in persulfate-based AOPs. *Environ. Sci. Technol.* **2025**, *59*, 17869-80. DOI PubMed
28. Wang, Y.; Liu, Y.; Zhang, H.; et al. Carbonaceous materials in structural dimensions for advanced oxidation processes. *Chem. Soc. Rev.* **2025**, *54*, 2436-82. DOI PubMed
29. Weng, Z.; Lin, Y.; Guo, S.; et al. Site engineering of covalent organic frameworks for regulating peroxymonosulfate activation to generate singlet oxygen with 100% selectivity. *Angew. Chem. Int. Ed. Engl.* **2023**, *62*, e202310934. DOI PubMed
30. Deng, Y.; Wang, S.; Zhou, T.; et al. Highly-separated Co anchored on S, O-doped carbon nitride for enhanced peroxymonosulfate activation: insights into radical and non-radical pathways. *Chem. Eng. J.* **2024**, *497*, 154580. DOI
31. Wang, Z.; Fang, Y.; Yang, Y.; Qiu, B.; Li, H. Vacancies-rich MOFs-derived magnetic CoFe encapsulated in N-doped carbon nanotubes as peroxymonosulfate activator for p-arsanilic acid removal. *Chem. Eng. J.* **2023**, *454*, 140474. DOI
32. Zhang, J.; Yu, G.; Zhang, Q.; et al. Spin-selection-favored peroxymonosulfate activation on reaction-induced Co-N_1O_2 sites enables $^1O_2$-biased yet radical-parallel oxidation. *Natl. Sci. Rev.* **2026**, *13*, nwag334. DOI PubMed PMC
33. Yu, G.; Zhao, W.; Wei, H.; et al. Bridge-bonded Mn-O-Mn interfaces decouple PMS adsorption from activation toward singlet-oxygen-selective water decontamination. *Appl. Catal. B:. Environ. Energy.* **2026**, *399*, 127100. DOI
34. Chen, M.; Yang, T.; Lei, Q.; Gan, X.; Mao, S.; Zhao, H. Constructing tandem Fenton-like reaction systems based on structure adaption to boost water contaminant mineralization efficiency. *Angew. Chem. Int. Ed. Engl.* **2025**, *64*, e202416921. DOI PubMed
35. Yang, P.; Cao, Z.; Long, Y.; et al. Regulating the local electronic structure of copper single atoms with unsaturated B,O-coordination for selective $^1O_2$ generation. *ACS. Catal.* **2023**, *13*, 12414-24. DOI
36. Zhang, L. S.; Jiang, X. H.; Zhong, Z. A.; et al. Carbon nitride supported high-loading Fe single-atom catalyst for activation of peroxymonosulfate to generate $^1O_2$ with 100% selectivity. *Angew. Chem. Int. Ed. Engl.* **2021**, *60*, 21751-5. DOI PubMed
37. Xiao, F.; Wang, Z.; Fan, J.; Majima, T.; Zhao, H.; Zhao, G. Selective electrocatalytic reduction of oxygen to hydroxyl radicals via 3-electron pathway with FeCo alloy encapsulated carbon aerogel for fast and complete removing pollutants. *Angew. Chem. Int. Ed. Engl.* **2021**, *60*, 10375-83. DOI PubMed
38. Zhao, Y.; An, H.; Feng, J.; Ren, Y.; Ma, J. Impact of crystal types of $AgFeO_2$ nanoparticles on the peroxymonosulfate activation in the water. *Environ. Sci. Technol.* **2019**, *53*, 4500-10. DOI PubMed
39. Zhang, J.; Liu, W.; Liu, B.; Duan, X.; Ao, Z.; Zhu, M. Is single-atom catalyzed peroxymonosulfate activation better? Coupling with metal oxide may be better. *Chin. J. Catal.* **2024**, *59*, 137-48. DOI
40. Zhang, M.; Xiao, C.; Yan, X.; et al. Efficient removal of organic pollutants by metal-organic framework derived Co/C yolk-shell nanoreactors: size-exclusion and confinement effect. *Environ. Sci. Technol.* **2020**, *54*, 10289-300. DOI PubMed
41. Liang, X.; Wang, D.; Zhao, Z.; Li, T.; Gao, Y.; Hu, C. Coordination number dependent catalytic activity of single-atom cobalt catalysts for Fenton-Like reaction. *Adv. Funct. Mater.* **2022**, *32*, 2203001. DOI
42. Zhao, Z.; Hu, M.; Nie, T.; et al. Improved electronic structure from spin-state reconstruction of a heteronuclear Fe-Co diatomic pair to boost the Fenton-like reaction. *Environ. Sci. Technol.* **2023**, *57*, 4556-67. DOI PubMed
43. Hu, L.; Zhang, G.; Liu, M.; Wang, Q.; Wang, P. Enhanced degradation of Bisphenol A (BPA) by peroxymonosulfate with Co_3O_4-Bi_2O_3 catalyst activation: effects of pH, inorganic anions, and water matrix. *Chem. Eng. J.* **2018**, *338*, 300-10. DOI

Disclaimer/Publisher's Note: All statements, opinions, and data contained in this publication are solely those of the individual author(s) and contributor(s) and do not necessarily reflect those of OAE and/or the editor(s). OAE and/or the editor(s) disclaim any responsibility for harm to persons or property resulting from the use of any ideas, methods, instructions, or products mentioned in the content.

© The Author(s) 2026. Open Access This article is licensed under a Creative Commons Attribution 4.0 International License (https://creativecommons.org/licenses/by/4.0/), which permits unrestricted use, sharing, adaptation, distribution and reproduction in any medium or format, for any purpose, even commercially, as long as you give appropriate credit to the original author(s) and the source, provide a link to the Creative Commons license, and indicate if changes were made.